JARO
Journal of the Association for Research in Otolaryngology

Tympanic Membrane Boundary Deformations Derived from Static Displacements Observed with Computerized Tomography in Human and Gerbil

STEFAN L. R. GEA,[1] WILLEM F. DECRAEMER,[1] ROBERT W. J. FUNNELL,[2,3] JORIS J. J. DIRCKX,[1] AND HANNES MAIER[4]

[1]Biomedical Physics, University of Antwerp, Groenenborgerlaan 171, 2020 Antwerp, Belgium

[2]Department of BioMedical Engineering, McGill University, Montréal, Canada

[3]Department of Otolaryngology, McGill University, Montréal, Canada

[4]HNO Universitätsklinikum Hamburg-Eppendorf, Martinistr. 52, 20246 Hamburg, Germany

ABSTRACT

The middle ear is too complex a system for its function to be fully understood with simple descriptive models. Realistic mathematical models must be used in which structural elements are represented by geometrically correct three-dimensional (3D) models with correct physical parameters and boundary conditions. In the past, the choice of boundary conditions could not be based on experimental evidence as no clear-cut data were available. We have, therefore, studied the deformation of the tympanic membrane (TM) at its boundaries using X-ray microscopic computed tomography in human and gerbil while static pressure was applied to the ear canal. The 3D models of the TM and its bony attachments were carefully made and used to measure the deformation of the TM with focus on the periphery and the manubrium attachment. For the pars flaccida of the gerbil, the boundary condition can, for the most part, be described as simply supported. For the human pars flaccida, the situation is more complicated: superiorly, the membrane contacts the underlying bone more and more when pushed further inward, and it gradually detaches from the wall when sucked outward. In gerbil, the attachment of the TM to the manubrium can be described as simply supported. In human, the manubrium is attached underneath the TM via the plica mallearis and the contact of the TM with the bone is indirect. For both human and gerbil, a simple boundary condition for the peripheral edge of the pars tensa is not appropriate due to the intricate structure at the edge: the TM thickens rapidly before continuing into the annulus fibrosis which finally makes contact with the bone.

Keywords: tympanic membrane, static pressure, deformation, boundary conditions, sulcus tympanicus, plica mallearis

Abbreviations: AF – annulus fibrosis (or fibrocartilaginous ring); EC – ear canal; PB – processus brevis (or lateral process); PF – pars flaccida; PM – plica mallearis (or mallear fold); PT – pars tensa; TM – tympanic membrane (or eardrum)

Correspondence to: Willem F. Decraemer · Biomedical Physics · University of Antwerp · Groenenborgerlaan 171, 2020 Antwerp, Belgium. Telephone: +32-3-2653430; fax: +32-3-2653318; email: wim. decraemer@ua.ac.be

INTRODUCTION

In the past, we have developed different moiré techniques with the main application being the measurement of tympanic membrane (TM) shape and deformation under static-pressure loads (e.g., Dirckx and Decraemer 2003, 2004). The moiré technique requires the object to be fully visible to permit projection of a regular grid (usually a line grating) onto the object and recording of this image

from a slightly different angle. To obtain a free view of the entire external surface of the TM, the bony ear canal (EC) has to be removed as close as possible to the annulus fibrosis (AF), but the tapering of the EC at its inferior end is so extreme that one cannot avoid having small remaining pieces of bone overhanging the TM. If the medial surface of the TM is exposed by opening the middle-ear cavity, the view of the TM and part of its boundary is obstructed by the middle-ear ossicles and, in some species (e.g., gerbil and guinea pig), by the cochlea.

More recently, we have also used X-ray microscopic computed tomography (micro-CT) to measure the intricate three-dimensional (3D) geometry of experimental ears and for the 3D description of middle-ear kinematics (Decraemer et al. 2003; Decraemer and Khanna 2004). X-ray CT is an imaging technique that produces a set of *virtual* serial sections of an object. Contrary to physical sectioning techniques, the sample is not destroyed and all section images are perfectly aligned. Conformation changes due to decalcification or cutting strain are avoided. Bone absorbs X-rays well and is, therefore, defined with high contrast and very dark gray levels; soft tissues such as the TM and ligaments have substantially smaller contrast and a lighter gray-scale value and can—sometimes with the help of some coating—also be outlined on the sections. The tomographic technique, therefore, permits us not only to study the full 3D shape of the TM from edge to edge, but also the 3D shape of its peripheral and central boundaries, namely, the AF and the manubrium. When the TM is subjected to a transtympanic pressure difference, CT permits us to study the details of the attachment of the TM to its boundaries.

These functional aspects of the boundaries are especially significant when mathematical models of the middle ear are formulated in an attempt to better understand the function of the middle ear qualitatively and quantitatively. The validity and usefulness of such models depend greatly on the fact that the parameters used in the model are known from a priori observations and are not based on mere assumptions nor estimated on the basis of fitting the model to indirect experimental results. Micro-CT can provide information on the nature of the boundary conditions for the TM that complements the measurements of membrane deformation that we obtained earlier with the moiré technique.

In this paper, we have used X-ray micro-CT to measure the displacement and deformation of the middle-ear components under static-pressure loads in human and gerbil ears. The gerbil ear is included in addition to the human ear because the gerbil is often used in experimental and modeling studies of the middle ear. We touch upon whole-TM deformations but concentrate on the description of the functional aspects of the boundaries.

ANATOMY OF THE TYMPANIC MEMBRANE WITH FOCUS ON THE BOUNDARIES

Structure and functional behavior are strongly interdependent so we start with a short overview of the anatomy of the TM, paying special attention to its connections at its boundaries.

General aspects

The TM in mammals consists of a thin membrane with two distinct parts, the pars tensa (PT) and the smaller pars flaccida (PF). The PF, the smaller most superior part of the TM, is slightly thicker and more lax. The PT has a somewhat conical shape as if drawn inward by the manubrium, which is coupled to the superior part of the PT. Nice illustrations of the human TM features can be found in classical textbooks (e.g., Anson and Donaldson 1981 or Gulya and Schuknecht 1995) and for gerbil in Figure 1A in the next section.

The PT is a layered membrane with a very specific internal organization featuring a thick outer epidermal layer, a thin inner mucosal layer, and a more substantial intermediate layer, the lamina propria (e.g., Lim 1970, 1995; Shimada and Lim 1971; von Unge et al. 1991). The lamina propria is composed of an outer subepidermal layer of connective tissue, a double layer of densely packed fibers, and another connective-tissue layer on the mucosal side. In the fiber layer, bundles of collagen fibrils are distributed in a highly organized way in radial (the outer layer) and circular (the inner layer) directions. Near the PF, some elastic fibers are also present.

The radial fibers generally run more or less straight from the manubrium to the AF. These fibers become more closely packed as they converge on the manubrium. The circular fibers mainly originate from the manubrium, describe an arc inferiorly around the umbo, and rejoin the manubrium on the other side. Most of them are attached to the manubrium fairly close to the superior end, near the short process. The circular-fiber layer is thinner than the radial layer, and near the umbo, it is very thin or even absent.

In the mid-area between the manubrium and the periphery, the thickness of the PT is very small and it increases very slowly both towards the annulus and towards the manubrium. PT thickness in human has been found to be very variable from individual to individual: using a precise confocal-microscope method, Kuypers et al. (2006) found, for three TMs studied, mean thickness values of 120, 50, and 40 μm. For gerbil, on the contrary, the thickness in the thinnest central zone was found to be about 7 μm, and this was remarkably similar for 11 different animals (although this might be influenced by the

fact that all samples were from animals belonging to the same strain; Kuypers et al. 2005). Although interspecies differences in size and shape of the PF are large, the PF always has essentially the same epithelial and mucosal lining as the PT (Lim 1968b). The lamina propria is generally thicker than in the PT and is dominated by loose connective tissue with randomly arranged collagen fibers (in contrast to the structured arrangement in the PT) and elastic fibers and an intricate external and internal vascular plexus of blood capillaries, arteries, veins, and nerve networks (Lim 1968a, b; Lim 1995).

In gerbil, the PF surface has small, irregular thickness variations. In the center, a mean thickness of ~23 μm was found; at a distance of between 100 and 200 μm from the edge, the thickness increases steeply to a value of ~82 μm (Kuypers et al. 2005). Measurements on human PF thickness differ a lot from one specimen to the other, as for the PT; Ruah et al. (1991) mention thickness values ranging between 80 and 600 μm, while Kuypers et al. (2006) report measurements between 50 and 140 μm.

Close to its peripheral edge, the PT thickness increases steeply (to a value of about 5.5 times that of the thinnest part in gerbil, 1.2 to 2.5 times in human) and the TM gradually merges into the AF. Most radial fibers pass directly into the AF; some of them cross each other just before entering the AF (Shimada and Lim 1971).

In the zone of the AF where it attaches to the bony tympanic ring, smooth muscle cells with radial orientation have been found in various species including both human and gerbil (Henson et al. 2005). These muscle cells may have a role in maintaining tension in the TM (Yang and Henson 2002), but in temporal bone (TB) preparations—as we used in our present study—any such tension was no longer present.

Pars tensa boundaries

Peripheral boundary. Among different species, the PT outer boundary varies from almost circular (e.g., human and guinea pig) to more or less elongate elliptical (e.g., cat and gerbil). Peripherally, the PT is
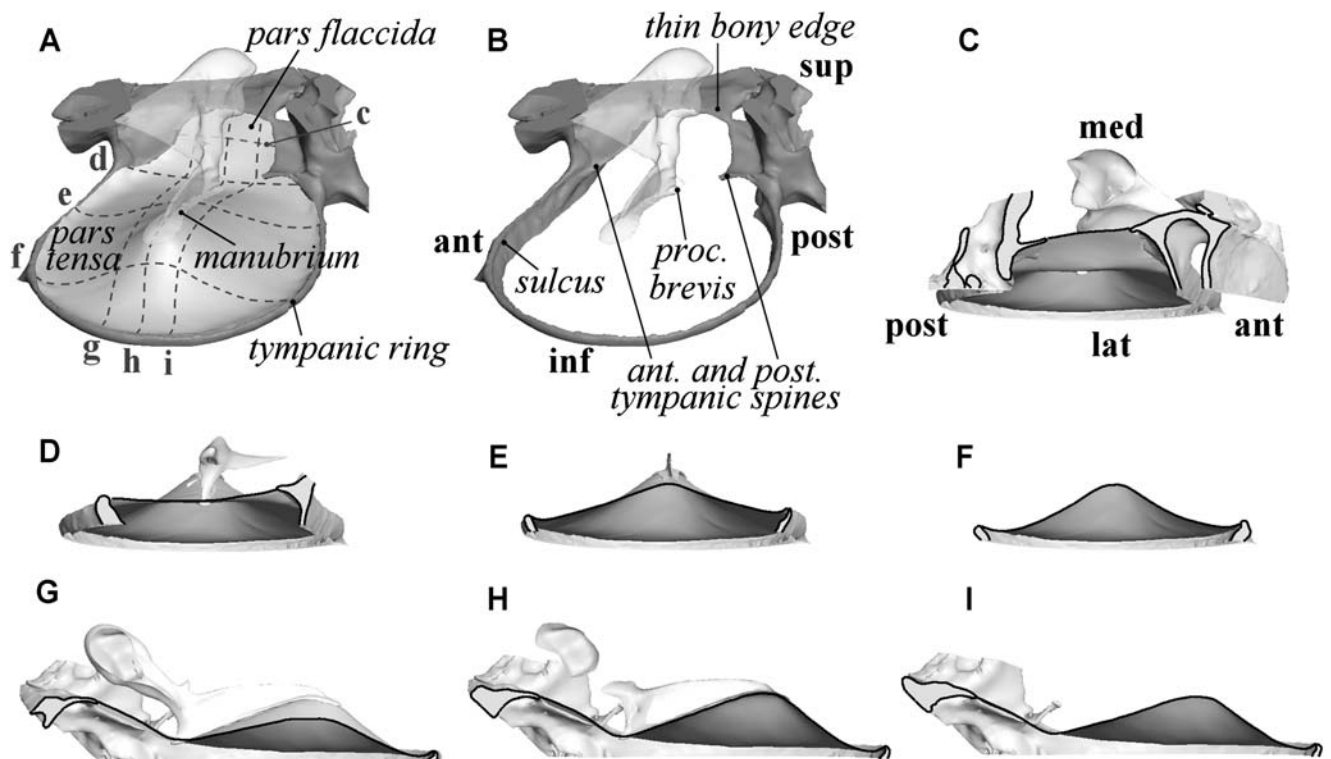
FIG. 1. 3D image of the TM of a gerbil (G2, right ear) within its bony support seen from the middle-ear side. In **B**, the TM was not drawn, revealing better the bony support. Relevant structures were annotated. In **C–I**, cross-sections of the model are shown with planes perpendicular to the annulus. In **C–F**, we look in a superior to inferior direction (from the PF down to the PT) at sections with planes perpendicular to the manubrium; parts in front of the section plane were removed. In the sections, the bone and the TM are outlined with *solid lines*. The locations were slices were made are shown in **A**. **C** Slices at a level at about the center of the PF, **D** at the level of the PB of the manubrium (neck of the malleus is visible), **E** at a midmanubrium level, and **F** at a level below the malleus tip. **G–I** The three sections parallel to the manubrium: **G** cuts anterior to the malleus, **H** along the center line of the manubrium, and **I** posterior to the manubrium. Further description can be found in the text.

bordered by the AF which is firmly anchored in the sulcus tympanicus, a groove in the bone of the tympanic ring. This ring of bone is incomplete at its upper part, ending at the anterior and posterior tympanic spines. From these spines, the anterior and posterior tympanic striae (also named "mallear" or "tympano-mallear folds" or "terminal arches") connect to the processus brevis (PB) of the malleus, the superior end of the manubrium. For example, for gerbil, these structures can be seen in Figure 1A, B. (We shall explain later how these figures were created.)

Kuijpers et al. (1999) and Uno (2000) show in the rat and guinea pig that the AF does not connect directly with the tympanic bone but via an interface of specialized connective tissue wherein the fiber bundles are dispersed into finer bundles before making contact with the bone of the sulcus tympanicus.

Manubrial boundary of the pars tensa. A thickening very similar to that observed at the peripheral edge is observed at the internal boundary with the manubrium (Kuypers et al. 2005, 2006). For guinea pig, Uno (2000) reports that, at the interface between the TM and the manubrium, the radial fiber bundles split into fine collagen bundles which then make contact with the edge of the flat top surface of the manubrium bone that is flush with the TM surface and can be observed through the EC. Based on the similarity in the way the manubrium is implanted in the TM in guinea pig and gerbil, we expect that this is most probably also true in gerbil.

The human manubrium has an elliptical cross-section which is entirely different from the T-beam structure in gerbil and other rodents. The attachment to the TM is also very different. Close to its inferior tip, the manubrium has an elliptical cross-section with its long axis parallel to the overlying TM, while more superiorly the long axis of the cross-section is perpendicular to the TM. Near the tip, the extremely thick fibrous lamina propria splits up equally to embrace the manubrium most intimately. The fibers in the layer wrap around both the medial and lateral faces of the manubrium and blend with the perichondrial layer overlying the cartilage surrounding the bony core of the manubrium.

Halfway up the manubrium, the TM sits lateral to the manubrium and the number of fibers in the lamina propria has become smaller. A significant portion of these fibers, compressed in an extremely thin layer, blend medially with the very thin perichondrium of the manubrium. In the literature (Politzer 1892; Graham et al. 1978; Gulya and Schuknecht 1995), the connection between the manubrium and TM is described as a thin "stalk" with a fibrous core, the plica mallearis (PM), covered by the mucosa of the middle ear. At its upper end, the manubrium is again firmly and closely connected to the PT.

Pars flaccida boundaries

Human. In human, the small, more or less triangular PF is a flush continuation of the EC wall and, from the EC, no distinct superior border can be seen. Superiorly, the PF detaches gradually from the petrous bone of the EC wall and, inferiorly, the border is formed by the anterior and posterior tympanic striae described above.

Gerbil. For gerbil, the anatomical details of the boundary to which the PF is attached are not well documented in the literature. The 3D models that we will use later to study the deformation of the TM at these boundaries provide information for describing the edge anatomy.

Figure 1A shows a 3D image of a (right) gerbil TM as it is held within its bony support as seen from the middle ear. In Figure 1B, the TM was left out in order to highlight the supporting structures. The figures demonstrate the circular shape of the gerbil PF. Figure 1A, G–I illustrate clearly that the PF plane is reclined backwards by about 30° with respect to the annulus plane, forming a crease (fold) between the PT and the PF at the level of the PB of the malleus. Figure 1C shows how the PF is attached to a thin bony ledge anteriorly and posteriorly and Figure 1G–I illustrate that this is also the case at the superior edge. The ledge starts at the anterior spine (more a broad inward bulge) and ends at the much finer posterior spine. Inferiorly, the PF is also attached to the top end of the manubrium (Fig. 1D). The anterior stria fills the fan-shaped gap between the upper edge of the PT, the lower circular edge of the PF, and the anterior end of the manubrium top. At the posterior end of the manubrium top, the posterior terminal stria connects to the posterior spine. The striae are thin membranes without any specific internal fiber organization (von Unge 2008, personal communication). Lim (1968b) mentions that some fibers from within the PF continue into the striae. The crease between PF and PT follows the upper edge of the terminal striae and reinforces the membranous part of the PF boundary, causing the *functional* peripheral border—where the displacement of the PF is zero (or nearly zero as we will see here) when overpressure or underpressure is applied to the PF—to be almost perfect circular (Dirckx et al. 1997).

MATERIALS AND METHODS

To measure the deformation of the TM under applied static pressure, with special interest in what happens

at the boundaries, we choose to use micro-CT scanning as it has the advantage that the measurement covers the entire membrane and is fully 3D. In human, the TM is sufficiently thick to be visible on the CT section images; for gerbils, the problem was circumvented by applying a small amount of water in the EC and letting it cover the TM. The water layer worked as a cast of the TM and showed up on the CT images.

Static pressures

To apply a static pressure over the TM, we used a device that was developed in-house and that provides pressures that remain stable (within a few pascals) over a long period of time using a feedback circuit (Dirckx et al. 1997). The pressure can be adjusted over a range of ±500 daPa in steps of 1 daPa. Pressures were applied through the EC, hence positive pressures in this paper refer to excess pressure in the EC; the middle-ear cavity remained at ambient pressure.

Micro-CT scanning

Human TBs were harvested as cores about 7 cm long and 3 to 4 cm wide. The bone is thick and has very dense parts. Because of the relative large size of the sample, the Skyscan 1076 in vivo μCT scanner was used. Gerbil TBs have extremely thin bone walls and have an overall size of about 1 cm. These samples were measured with the Skyscan 1072 that provided slightly better spatial resolution. We verified in a preliminary test that it was sufficient to wait a few minutes after the pressure was applied to let the creep practically die out and then start the CT scan.

Scanners and scan parameter settings

The Skyscan 1072 is equipped with a fixed source–detector setup and the sample is mounted between the source and detector on a rotational stage. By moving this stage forward or backward, the magnification can be chosen. At the lowest magnification level (×14.14) the maximal field of view is ~2 cm, which is about what is required for a conventional scan of the gerbil TB. We have shown that region-of-interest (ROI) tomography can be used to zoom in on parts of the specimen while allowing other parts of the object to move out of the X-ray beam during the scan recording (Gea et al. 2005). We showed that, in this way, the spatial resolution could be considerably improved and small details, not visible in a regular full-object scan, can be revealed by a ROI scan, while geometrical information remains unaffected. A magnification of ×45 could be used, resulting in a geometrical resolution of 6.53 μm per pixel. The scanning parameters were chosen to reduce the

scanning time (~30 min) while retaining good quality of the reconstruction images. The X-ray source was set at maximal power output (80 kV, 100 μA), while 138 images with averaging over two frames were recorded over an angular interval of 180° (angular step 1.3°). The Plexiglas container in which the TBs were mounted had the beneficial side effect that beam-hardening effects were greatly reduced so that the standard aluminum beam-hardening filter could be omitted and the exposure time could be reduced to 2 s per acquisition, considerably reducing the total recording time per applied pressure to about half an hour.

In contrast to the 1072, the Skyscan 1076 in vivo μCT scanner has a classical CT setup, i.e., a fixed sample bed with the source and diametrically opposite detector rotating about the sample. Two sample beds with diameters of 38 and 65 mm are available to hold samples of different sizes. For this study, the smaller bed was used. Beam-hardening effects and image noise were reduced with a 1-mm aluminum filter and by averaging over ten images. The power output was set to maximum (100 kV, 100 μA) and a rotation step of 0.6° with a total angular rotation of 180° was chosen. The image magnification for this scanner is fixed, with a pixel size of about 9 μm. A pixel size of 18 or 35 μm can be selected by binning 2×2 or 4×4 pixels; this "averaging option" reduces the scanning time by a factor of approximately 2 to 4, as well as reducing scanning deficiencies such as ring artifacts. It is mainly for the former reason that the sample was scanned with a pixel size of 35 μm, leading to an exposure time of 474 ms per frame and a total scanning time of 30 min for each pressure step.

Human temporal bones

Measurements were performed on two human TBs that were obtained from the Universitätsklinikum Hamburg-Eppendorf and collected on the basis of the Hamburg Autopsy Law from February 9, 2000. The donors died of non-ear-related causes; TB1: right ear, age 72, male; TB2: right ear, age 34, female. Tympanograms recorded immediately after dissection of the TB showed no abnormalities. The TBs were wrapped in a cloth moistened with saline and kept in a plastic bag to prevent dehydration. During transport from Hamburg to Antwerp, the samples were kept at a temperature of a few degrees Celsius in a cooler. In Antwerp, the TBs were slightly trimmed down to fit the 38-mm-wide scanning bed of the in vivo μCT scanner. Care was taken not to disrupt the cochlear and vestibular systems. For the scan, the TBs were wrapped in Parafilm (to avoid desiccation) and firmly secured in the scanner bed with adhesive tape. The entire process of dissecting, transporting, preparing, and scanning was completed within 24 h (TB1) and 48 h (TB2) postmortem.

To apply the pressure to the ear, the flexible tube from the pressure device was passed through an ear plug firmly glued into the EC. As no effort was done to seal the middle-ear cavity—human TBs always have leaks to the middle ear—the middle ear was at ambient pressure during the entire experiment. Before the scanning sequence was started, the pressure was within about a minute swept twice between −500 and +500 daPa as a preconditioning stage.

TB1 was scanned seven times following the pressure cycle: 0, −100, +100, −200, +200, −500, and +500 daPa. TB2 was scanned at a few more pressure steps (11 in total): 0, −50, +50, −100, +100, −200, +200, −300, +300, −490, and +490 daPa.

Gerbil temporal bones

Two adult female Mongolian gerbils (*Meriones unguiculatus*) were sacrificed using carbon oxide gas; they were decapitated and their TBs (with intact cochlea and vestibular system) were carefully removed (G1, left ear; G2, right ear). We checked that the ears had pristine TMs. During preparation, the TBs were continuously moistened by working in mist of an ultrasonic humidifier (Bonaire BT-204) directed via a plastic tube (a few centimeters in diameter) onto the specimen. A small perforation was made in the bulla to avoid pressure build-up in the middle ear. A Plexiglas tube (outer diameter 6 mm, inner diameter 3.5 mm) was glued hermetically over the entrance of the EC. Care was taken that glue did not enter the EC. The Plexiglas tube was used to connect via a flexible plastic tube to the pressure device and to hold the specimen in a thin-walled plastic container that was mounted on the rotation stage of the micro-CT scanner such that the plastic tube did not obstruct the rotation motion. A small drop of water was put in the EC and allowed to run onto the TM in order to visualize the position of the otherwise too-thin TM in the X-ray images. The gerbil bullar bone was sufficiently thin that, during the preconditioning pressure sweep, we could follow the displacements of the malleus tip on a highly magnified shadow X-ray image. This way we could also check whether all connections were well sealed. Both ears were scanned with the same pressure sequence of 0, −20, +20, −50, +50, −100, +100, −200, and +200 daPa. The first scan started half an hour postmortem; the last one ended 5 h later.

Segmentation, 3D modeling, and data representation

Data in our experiments were collected as stacks of serial sections obtained from the reconstruction of the micro-CT images. The section images were segmented to construct 3D models of the middle-ear structures (TM, PM, and ossicles). The sectional images were also used directly to look, e.g., at displacements of structures in cross-sections. During segmentation, structures are identified with contours in consecutive sections and specialized software is finally used to produce the 3D model of the structure that is analyzed. In a previous paper, we have reviewed some segmentation algorithms and the software packages that implement those (Decraemer et al. 2003).

For the present paper, we have used the packages SurfDiver and Amira for the segmentation and model building. To obtain cross-sections in directions different from the coordinate planes in the section data stack, reslicing was performed using Amira (e.g., the cross-sections of the TM with differently oriented planes shown in Figures 4A–E and 5A–E were obtained this way). For the data presentation, Matlab, Amira, and Mesh3D (Maas, 2005, personal communication) were used.

RESULTS

Human

Anatomy of the manubrium–tympanic membrane attachment (plica mallearis). In the anatomical introduction, we discussed how in human the manubrium is rod-like and attached underneath the TM by the PM, while in gerbil (and many other laboratory animals) the manubrium has a T-beam-like structure which is attached along its flat top part to the TM.

Current information on the attachment of the human manubrium to the TM is essentially based on histological sections (Politzer 1892; Graham et al. 1978; Gulya and Schuknecht 1995). Depending on the source, three to four sections are shown, e.g., at the umbo, at the PB, and at a few intermediate locations, but a complete view is not shown.

With the information in the stack of section images from a whole middle-ear CT scan, we were able to construct a 3D model of the entire manubrium, the PM, and the overlying external surface of the TM to show precisely the anatomical relation of the TM to the manubrium in our specimens. In Figure 2, we have made a compilation of different views and aspects of this 3D model based on the scan data for TB1 at −500 daPa. At first, it seems that it would have been preferable to have used the data set at zero pressure, but unfortunately, the segmentation in that set especially at the PB was not clear-cut. With regard to the discrepancy in width between our PM model and the histological description from the literature—which we will describe later—we will see that the use of the most negative pressure data set was finally not a bad choice. Section images for TB2 showed that its PM had a width comparable to that for TB1, indicat-
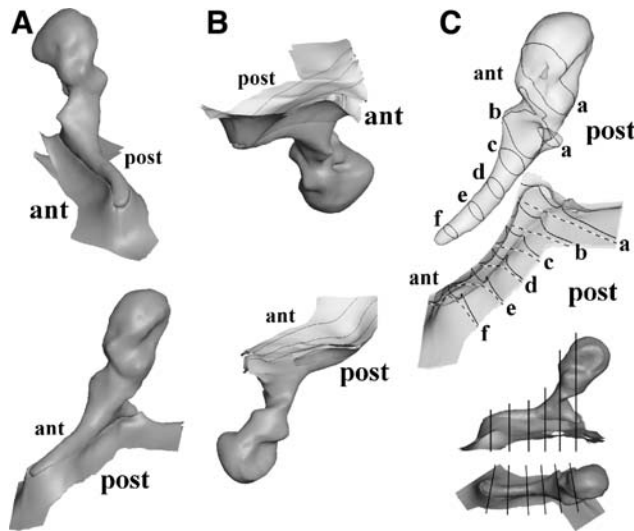
FIG. 2. **A** The anterior and posterior views of the medial aspect of a 3D model of TB1 (right ear) comprising the malleus, the PM making the connection between the manubrium and the TM, and the onset of the TM anteriorly and posteriorly; the remaining part of the TM was left out for clarity. **B** The anterior and posterior views of the lateral aspect of the model show that the external surface of the TM is quite flat with hardly a trace indicating where the manubrium is attached below. **C** The malleus and PM model were enlarged and separated from each other to better illustrate anatomical details of both structures and their zone of contact. Width and thickness of the PM can be judged from cross-sections with planes perpendicular to the long axis of the manubrium taken at locations labeled *a* to *f* (shown also on the right of **C**). Please refer to the text for more details.

ing that the one model made is illustrative for the two human TBs studied.

Figure 2A (left column) has an anterior and posterior view of a 3D model composed of the malleus, the PM making the connection between the manubrium and the TM, and the onset of the TM anteriorly and posteriorly; the remaining part of the TM was not shown for clarity. Figure 2B (middle column) shows that the external surface of the TM is quite flat and that looking through the EC one cannot see where the manubrium is attached below. (The three thin lines on the external TM surface are fictitious sections with parallel planes to give a better idea of the surface curvature.)

In Figure 2C (right column), the malleus and PM are shown at a larger magnification and were separated from each other to better show the anatomy of both structures individually and of their zone of contact. To clearly illustrate some characteristics of the PM, especially its width and thickness, cross-sections with planes perpendicular to the long axis of the manubrium, taken at locations labeled a to f (as shown in the smaller drawing at the bottom of panel C) are also shown. The sections of the manubrium and of the lateral (solid line) and medial side (dashed line) of the PM are drawn on the respective models.

The PM has a groove that embraces the manubrium all the way from the umbo to the PB. The delineation of the upper anterior and posterior edge of the PM of our model are open to interpretation as it is hard to decide on a CT section (or even on a stained histological slide) where the PM ends and where the epithelium and fibrous layer that encircles the manubrium starts. During segmentation of the PM, we stopped where it became too thin to be discriminated, which resulted in the PM model shown that embraces the manubrium over one third to half of its circumference. Below the groove, the PM stalk narrows slightly down (mainly at section c of panel C) to widen again all along its length to contact with the overlying TM.

The shape of the cross-section of the manubrium changes along the manubrium length as described in the anatomical overview above. The distance between the external surface of the TM and the manubrium was smallest in the umbo region (section f=~150 μm) and increased when moving closer to the PB (sections e=~270, d=~330, c=~680, and b=~815 μm), while right at the lateral process, it has decreased again (section a= ~440 μm). The width of the PM was smallest at midmanubrium (sections c=680 μm and d=540 μm). It was almost equal to the width of the manubrium (i.e., the short axis of the elliptical cross-section) in section c and was slightly smaller than this in section d.

The distance between the TM and the manubrium is in agreement with histological findings, but in our model, the PM is considerably wider than what was seen on histological sections where in the midzone (corresponding to our sections c and d) it showed up as a "thread" about one fifth of the width of the underlying manubrium (Politzer 1892; Graham et al. 1978; Gulya and Schuknecht 1995). As mentioned earlier, our
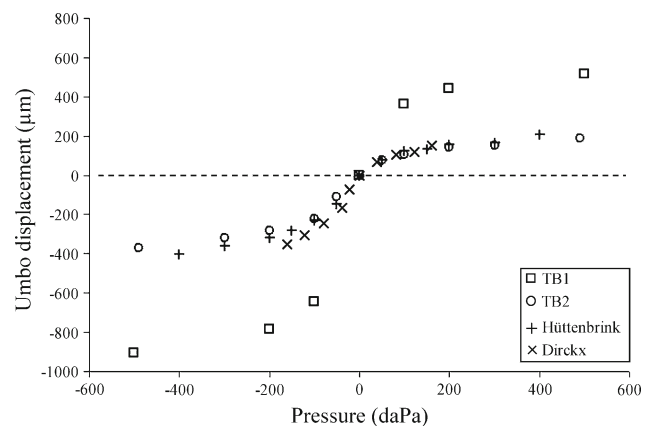
FIG. 3. Displacement of the malleus tip is shown for two right human TBs: TB1 (*open squares*) and TB2 (*open circles*).For TB2, good agreement is found with data from Hüttenbrink (1988) based on radiographic images of the ossicles under pressure loads from 0 to ±400 daPa (*plus symbols*) and with data from Dirckx and Decraemer (1991) obtained with moiré topography over a range of ±160 daPa (*cross symbols*). For TB1, the displacement was considerably larger.

model was made using the −500-daPa data set that should have captured the PM in a stretched and thinned configuration. This discrepancy in width could be caused by (1) shrinking effects during the histological preparation or (2) moisture that had collected in the constriction and showed up on the CT images with a contrast similar to that of the tissue of the PM; probably both effects could have played a role in making the histological width smaller and the CT width larger. The observations of the TM deformation at the central boundary and the conclusions that we base upon it will be discussed in the light of this discrepancy.

Malleus tip displacement. 3D models of the malleus were made for all different pressure data sets. Displacement for a given landmark could then easily be calculated as the magnitude of the 3D displacement vector for this point. Displacement values of the malleus tip are shown in Figure 3 (open squares, TB1; open circles, TB2). For comparison, we also show with plus symbols data from the literature by Hüttenbrink (1988) based on radiographic images of the ossicles under pressure loads from 0 to ±400 daPa and with cross symbols data by Dirckx and Decraemer (1991) obtained with moiré topography over a range of ±160 daPa. The TM layer covering the manubrium at its tip is thin and the connection to the TM is very tight—Gulya and Schuknecht (1995) emphasize this tight connection: "At the umbo the lamina propria splits to envelop the malleus, making it difficult to separate the malleus from the tympanic membrane without perforation"—so that at this place the TM covering the malleus tip follows the underlying bone closely. (That this is indeed so will be shown below in Figure 6 of the "Deformation of the plica mallearis" section.) All curves display a large asymmetry for positive and negative pressures with a leveling off of the pressure–displacement curve at high pressures. Our measurements for TB2 are quantitatively in good agreement with the measurements of Hüttenbrink and Dirckx et al. with plateau values of −370 and 190 µm, while TB1 shows a three times larger umbo displacement (plateau values=−908 and 514 µm). Although the reason for this large difference is unclear, the ratio between the outward and inward umbo movement is 1.8 for TB1 and 1.9 for TB2, which is almost identical to the value of 1.9 found by Hüttenbrink and Dirckx et al.

The points of agreement in the displacement versus pressure curves with literature validate the present measurement technique; the fact that substantial umbo displacements were measured is further a strong indication that the specimens had not dried out during the experiments.

Deformation of the annulus fibrosis. To observe the deformation of the AF, cross-sections perpendicular
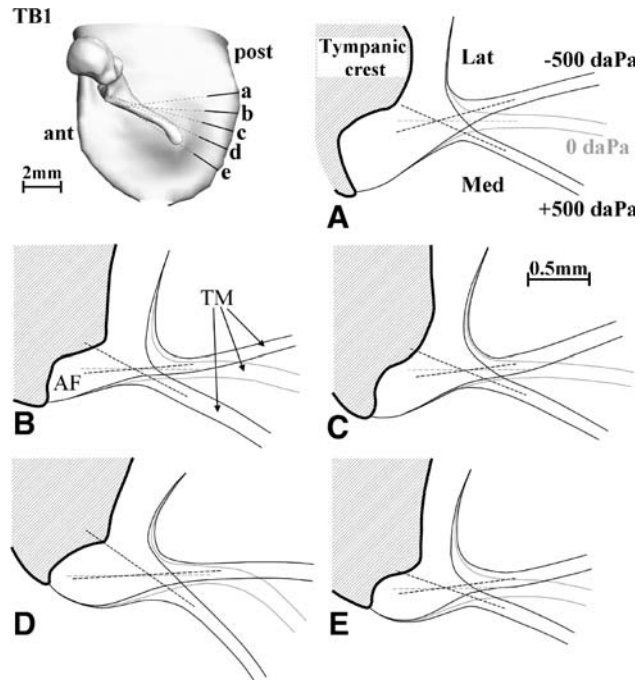
FIG. 4. Cross-sections perpendicular to the annulus plane and orthogonal to the annulus boundary for −500, 0, and +500 daPa show the deformation at the peripheral boundary for TB1 (right ear). The location and orientation of the sections are indicated on the 3D models in the *upper left corner*. The *dashed lines* represent the midline of the TM at the edges just before it merges with the AF. When extrapolated, the lines for different pressures intersect at a single point. The point is situated at the base of the triangular thickening zone of the TM where it blends into the AF.

to the annulus plane and orthogonal to the annulus boundary were obtained after reslicing the 3D image stacks resulting from the CT scans. Sections for zero and for maximal positive and minimal negative applied pressures were made by precise manual segmentation. The location and orientation of the sections are indicated on the 3D models in the upper left corner of Figures 4 and 5. The deformation of the AF and the adjacent part of the TM can be seen in Figures 4A–E and 5A–E. Annotations indicate the rest position (0 daPa) and the positions for minimal (−500 daPa) and maximal (+500 daPa) pressure position. The dashed lines represent the midline of the TM at the edges just before it merges with the AF. These were extrapolated to let the lines for different pressures intersect. In most cases, the three lines intersect at a single point or nearly so (Fig. 5A, B). The point is situated at the base of the triangular thickening zone of the TM where it blends into the AF.

Let us remark also that, on the cross-sections a to e, we can observe the rather thick epithelium layer (~0.25 mm) on the bony EC wall (lateral), while the mucous layer on the bone of the middle ear is not shown as it is so thin that it could not be segmented as a separate layer.
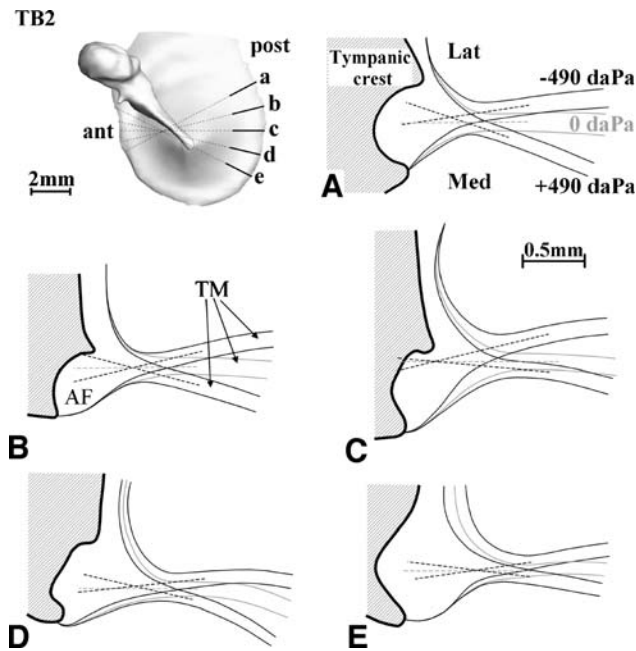
FIG. 5. Figure for TB2 (right ear), with layout similar to Figure 4. Extreme EC pressures here were ±490 daPa, slightly different from those in Figure 4. Except in **A** and **D**, the extrapolated lines for different pressures again intersect at a single point or nearly so.

Boundary conditions. In mathematical studies of deformations of membranes, plates, or shells, various boundary conditions are commonly formulated. A first condition to be met at a fixed edge is zero displacement at the boundary. A second condition can specify whether the edge is *simply supported* (or *hinged*) or *fully clamped*, i.e., whether the slope of the structure at the boundary changes when the plate is deformed or not. The *simply supported* condition is equivalent to assuming that the rotational degrees of freedom are not constrained at the boundary, while the *fully clamped* condition implies that the rotational degrees of freedom are constrained to be zero at the boundary.

We showed in Figures 4 and 5 that the midline of the PT performs a rotation about a point at the edge between PT and AF; with this simplification of only considering the midline, the PT would have a *simply supported* boundary, not at the bony edge with the sulcus, but at the transition between PT and AF. From Figures 4 and 5, it is clear, however, that in reality the PT undergoes a bending deformation in the entire wedge region where it thickens considerably and merges with the AF. Such a deformation is different from what we expect for a thin plate under either *simply supported* or *fully clamped* conditions. We see that the mathematical classes used for the boundary description of plates can only in a gross approximation describe the fine details of the deformation of the TM at its peripheral border.

Deformation of the plica mallearis. We studied the deformation of the PM as a function of pressure in a plane cross-sectioning the manubrium along its length in a direction perpendicular to the annulus. The intersection of this plane with the TM and malleus can be seen in the upper left panel of Figure 6 while the cross-sections of the TM and the malleus are shown for 0, +500, and −500 daPa in the other quadrants of the figure. Results for TB1 are shown.

Because the chosen section plane is fixed in space for every pressure, one can notice slightly different contours of the malleus. The middle-ear ossicles indeed do not describe a pure rotational movement around a fixed axis perpendicular to the image plane, but a more complex 3D movement, hence the contour of the malleus in a fixed cross-section plane (chosen at zero pressure) changes slightly as the malleus is displaced. For positive pressures, the umbo is pushed inward and the malleus cross-section rotates clockwise about the umbo in the figure plane of Figure 6; for negative pressures, the rotation is counterclockwise.

We note also that the distance between the manubrium and the external surface of the TM changes with pressure. At positive pressures, the TM pushes against the manubrium and comes in close contact with it all along its length, which causes a strong outward bump of the TM at the PB. At negative
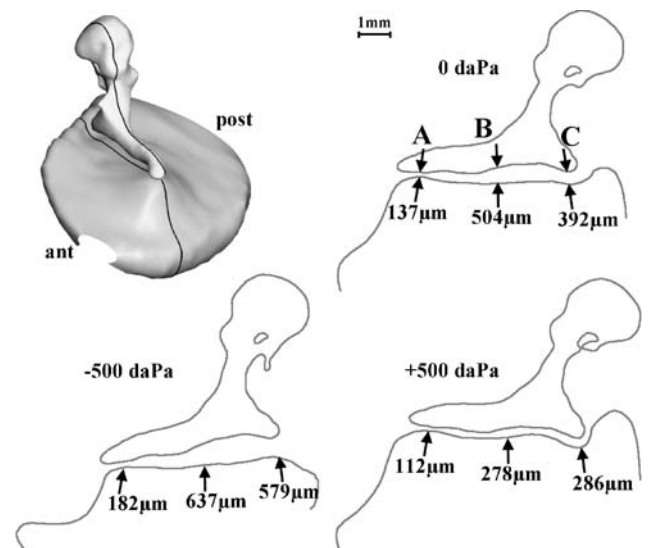
FIG. 6. Deformation of the PM of TB1 (right ear) as a function of pressure in a plane sectioning the manubrium along its length in a direction perpendicular to the annulus. The *upper left panel* shows the intersection of this plane with the TM and malleus. Cross-sections of the TM and the malleus are shown for 0, +500, and −500 daPa in the other three quadrants. For positive pressures, the umbo is pushed inward and the malleus cross-section rotates clockwise about the umbo in the figure plane; for negative pressures, the rotation is counterclockwise.

pressures, the distance widens and becomes largest at the PB and the bump reverses. The connection between the malleus and the PT is seen to be the most firm at the umbo, resulting in a motion of the malleus that resembles that of a cross-country shoe flexibly connected to a ski at its tip.

For TB1, the distances between the manubrium and the lateral side of the TM were annotated in Figure 6 at three locations along the manubrium. The distance at the umbo (point A) hardly decreases when EC pressure is increased from 0 to +500 daPa (from 137 to 112 μm, a change of −25 μm); for a pressure decrease from 0 to −500 daPa, the distance increases to a greater extent (from 137 to 182 μm, a change of +45 μm). The PB (point C) on the other hand moves away from the TM over a distance of 187 μm (579 and −392 μm) at the negative pressure and approaches by −106 μm (286 and −392 μm) at the positive EC pressure. The point halfway along the manubrium (point B) shows a similar behavior: there was an increase of the distance by +133 μm at the negative pressure and a decrease by −226 μm at the positive pressure. TB2 was not useful for this kind of calculation since part of the TM at the site of the malleus handle was covered with fluid at zero pressure (probably caused by a postmortem effect), so we could not make a precise segmentation of the lateral surface of the TM.

Inspection of an additional CT data set from a human TB with an implanted middle-ear prosthesis (Otologics, MET™) contacting the body of the incus to an electromagnetic driver—which should not have altered the PM behavior—also showed a decrease in distance between the manubrium and the lateral side of the TM at the positive EC pressures: at the umbo 0 μm, at midmanubrium −13 μm, and at the PB −119 μm; at the negative pressure the distance widened by +132 μm at the umbo, +203 μm at midmanubrium, and +346 μm at the PB. The result for the positive pressures indicates that the connection between the manubrium and the TM was not as tight as for TB1, indicating inter-individual differences of this aspect.

Pars flaccida. We were not successful in making 3D models of the human pars flaccida. It looked as if one of the superficial layers had separated from the underlying surface during the relatively long exposure to the static pressure. This made segmentation and subsequent analysis impossible. In the "Discussion" section, we will show that we can fill in this gap quite nicely using some of our older moiré results.

Gerbil

General observations. As mentioned earlier, a small amount of water was dropped into the EC to form a
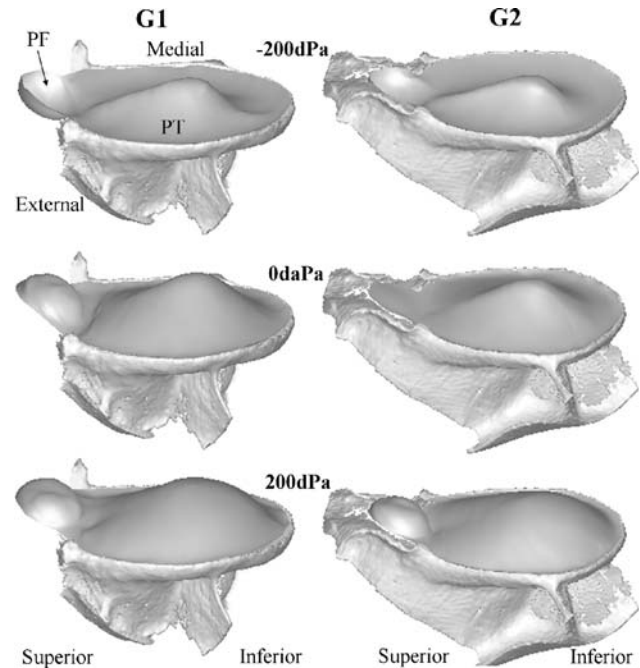
FIG. 7. 3D models of the TM for gerbils G1 (left ear) and G2 (right ear) at zero pressure (*middle row*), most negative pressure (*top row*), and most positive pressure (*bottom row*) illustrate the resting and deformed shape. The anatomy of the tympanic ring, which, as a thin band structure at the end of the external EC, provides the peripheral support for the TM, is clearly seen. Only for G2, the bony ledge of the PF is shown. This figure nicely illustrates how the PF deforms into a spherical cap.

thin liquid making the external TM surface visible on the CT sections. As a drawback, the AF and the epidermal layer on the EC wall, showing up with the same gray level as the thin water layer in the EC, could not be distinguished from the water during segmentation. Consequently, in the 3D models that were made for gerbil, we could only introduce the external surface of the TM and the AF edge. For the TM, this is not really a drawback as the TM is extremely thin in gerbil, but it makes it impossible to follow the deformation of the AF as we could do in human. Let us emphasize, in view of the discussion of the deformation at the edge that will be given below, that the peripheral bone was very distinct and could be precisely segmented.

Two data sets (for animals G1, left ear and G2, right ear) were available with complete pressure cycle recordings at 0, ±20, ±50, ±100, and ±200 daPa. Figure 7 shows the models at zero pressure (middle row), minimal pressure (top row), and maximal pressure (bottom row). The larger part to the left is the PT modeled all the way to the annulus. As mentioned above, only the external surface of the TM was segmented, so what is shown here is a medial view of this surface (which is why the manubrium is not seen). We see how the PT is pushed laterally for negative EC pressure and medially for positive pres-

sure, changing the depth and the curvature of the cone. The figures for G1 and G2 also clearly show the anatomy of the tympanic ring, which, as a thin band structure at the end of the external EC, provides the peripheral support for the TM.

The smaller circular cup-like part at the right is the PF; for G2, its bony support is also shown. It can be seen that the PF of G1 is already deformed even when no external pressure is applied in the EC. Although this could be the result of putting water into the EC, causing a small initial pressure (~5 daPa), this is contradicted by the result for animal G2 with a much smaller initial deformation. The same phenomena of an outward or inward bulged PF with no pressure load applied was also seen by Dirckx et al. (1998) who studied the PF deformation as a function of pressure with a moiré interferometer in a gerbil TB preparation with intact middle and inner ear. Some PFs never became perfectly

flat at all, but suddenly flipped over when the pressure changed to a small negative value. Here also, for both G1 and G2, the PF was sucked outward as soon as the slightest negative EC pressure step was applied.

Remark also in Figure 7 how the crease between the PT and the PF continues the circular bony boundary of the PF and that, when the TM is pressurized, only a slight deformation takes place in this zone.

Deformation of the pars tensa. 3D models of the manubrium, the TM, and its bony circumferential support were made for all pressure load configurations. Figure 8 shows, for G1 (at the left) and G2 (at the right), profiles of the models for the TM and their supporting bony rim taken in an anterior–posterior direction, perpendicular to the manubrium (a to f), and one in an inferior–superior direction (g). On the 3D models in the middle (view from the middle
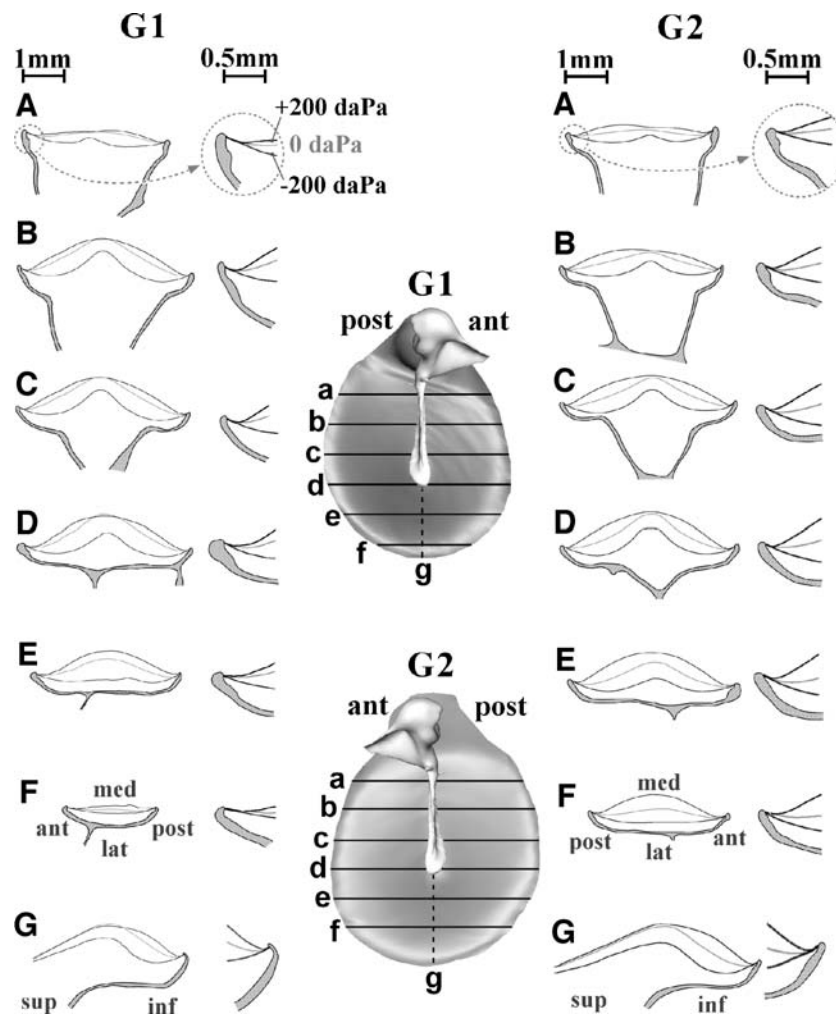
FIG. 8. Cross-sections of the models for the TM of G1 (left ear) and G2 (right ear) and their bony rim in an anterior–posterior direction, perpendicular to the manubrium (**A** to **F**), and in an inferior–superior direction (**G**). Enlargements of the profiles at the annulus edge are also shown. For +200 daPa EC pressure, the profiles crossing the manubrium (**A** to **D**) show that the manubrium moved little from its 0 daPa position, while the free parts of the TM changed their curvature from convex outward to concave outward. For −200 daPa, the manubrium had a considerably lateral displacement and the convex outward curvature of the TM was increased.
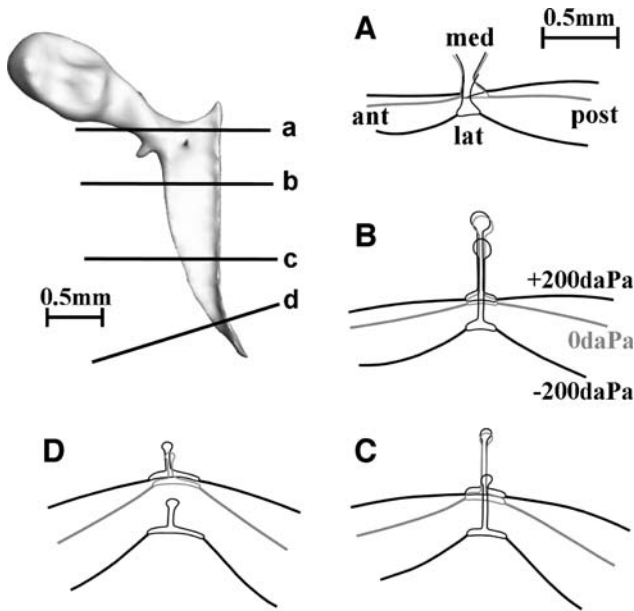
FIG. 9. Four cross-sections perpendicular to the manubrium top surface are shown (labeled *a* to *d* on the malleus model at the *top left*) for the rest position (*middle line*) and for pressure loads of +200 daPa (displacement in medial direction) and −200 daPa (in lateral direction). Remark how in gerbil the flat lateral surface of the manubrium is embedded in the TM. Under pressure load, the TM hinged about its attachment to the manubrium and the TM deformation relative to the manubrium can hence be classified as simply supported.

ear), the locations where the profiles were taken are shown annotated with letters a to g. In each subpanel, a to g, are plotted profiles and inserts with enlargements of the profiles at the annulus edge. For an overpressure of +200 daPa in the EC, the profiles crossing the manubrium (panels a to d) show that the manubrium was nearly blocked in comparison to the TM in its 0 daPa position while the free parts of the TM changed their curvature from convex outward to concave outward. For an underpressure of −200 daPa in the EC, the manubrium moved considerably laterally and the convex outward curvature of the TM became more pronounced. This is in accordance with results from Dirckx and Decraemer (2003).

Deformation of the pars tensa at the peripheral edge. The enlargements in Figure 8 show that the TMs of G1 and G2 are not deformed in a small region of about of 100 to 150 μm directly neighboring the bony edge (not so clear in G1e and G2f); this is true both in the sections perpendicular to the manubrium and in the section along the manubrium direction. The edge between membrane and bone was well defined on the sections, so we are certain that the small ring where no deformation is seen is part of the TM and not of the bone. At the inner edge of this ring, the TM has a quite sudden onset of the deformation (nearly hinge-like, conforming to the *simply supported* BC) and further

inward from this point there is also a gradual bending of the membrane. The width of this ring coincides with a local thickening of the TM that was reported by Kuypers et al. (2005) in her gerbil thickness study: "Near the manubrium and the annulus, thickness increases steeply. At a small distance from the annular edge, a pronounced local bulge was observed."

Coming to the conclusion that we can assign a *simply supported* BC to the TM not at the bony edge with the sulcus but rather at the inner edge of the peripheral bulge in the TM shows again that it is not straightforward to decide unequivocally about a mathematical class of boundary condition on the base of a deformation profile when the thickness of the membrane is so variable close to the edge.

Deformation of the tympanic membrane at the manubrium edge. The 3D models of the manubrium and the TM were also used to draw the four cross-sections perpendicular to the manubrium top surface shown in Figure 9 (labeled a to d on the malleus model at the top left) for the rest position and for the extreme pressure loads ±200 daPa. In gerbil, the flat lateral surface of the manubrium is embedded in the TM all along the length of the manubrium. In Figure 9, we see again that the malleus moved laterally when a negative EC pressure was applied but hardly any movement was observed for a positive pressure. Under pressure load, the TM hinged about the points where it connects to the manubrium: the TM deformation relative to the manubrium can be classified as *simply supported.*

Volume displacement of the pars tensa. The volume displacements of the PT were calculated based on the 3D TM displacement. Results are shown in
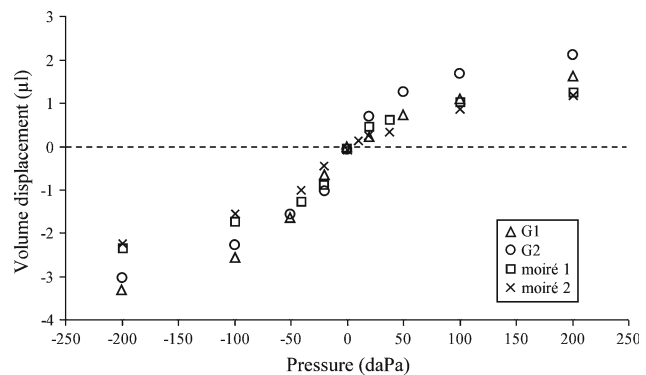
FIG. 10. Volume displacements of the PT calculated using the 3D TM displacement, compared with moiré measurements. The displacement levels off for extreme pressures: +1.5 and −3.4 μl for G1 at +200 and −200 daPa respectively, and comparable values of +2.1 and −3.1 μl for G2. Old unpublished moiré-shift measurements were also used to calculate PT volume displacements for both positive and negative pressure. For comparison, such data for two gerbils are shown.

Figure 10. The displacements level off for extreme pressures: we found +1.5 and −3.4 µl for G1 at +200 and −200 daPa, respectively, and comparable values of +2.1 and −3.1 µl for G2. We have also revisited measurements that we did years ago using a moiré-shift interferometer (Dirckx and Decraemer 1991) on gerbil preparations similar to those used for the real-time moiré measurements of PT displacement we did with von Unge et al. (1993). Based on moiré measurements for two gerbils, PT volume displacements were calculated for positive and negative EC pressures and the results are plotted for comparison in Figure 10. Curves for G1 and G2 are comparable to those for the moiré measurements albeit that the present volume displacement values are somewhat larger.

The somewhat larger volume displacements of the PT found in this study, compared to our older moiré studies, are probably due to the much longer exposure to each pressure step than in the rapid moiré measurements (~30 min per pressure step compared to 10 s). In both cases, the accumulated creep in the soft viscoelastic PT is thought to be at the origin of the larger deformations.

Deformation of the pars flaccida. The structure and composition of the PF is very different from the PT. The mechanical properties of the membrane are, therefore, different as well which will also strongly influence boundary phenomena. At the top left of Figure 11, we have shown where four radial cross-sections (a–a′ to d–d′) of the PF were taken. Profiles in Figure 11 are shown for the PF in its position for extreme pressures of ±200 daPa and for the rest position. Notice that the points a, b, c, d, and a′ are at an edge with the bone, while points b′, c′, and d′ are points on the crease between PT and PF. For the negative EC pressure, the PF has a nearly symmetrical profile. For the positive pressure, the profiles show an indent indicating where the PF made contact with the malleus head. Dirckx et al. (1997, 1998) did not find such a phenomenon, although the pressure range was identical. At the bony ledge, the PF displays a *simply supported* boundary condition. At the crease between the PF and the PT (b′, c′, and d′), the boundary is not perfectly fixed. The deflection at the boundary at points b′ and d′ shows nearly constant slope at the edge; this is also true at point c′, but here the nearness of the bone of the manubrium top blocks inward deflection of the membrane. A simply supported or fully clamped boundary condition in this zone is not appropriate.

Volume displacement of the pars flaccida. In this study, we found PF volume displacements of −0.52 µl (G1) and −0.63 µl (G2) at −200 daPa and +0.71 µl (G1) and +0.51 µl (G2) at +200 daPa. Dirckx et al. (1998) found displacements leveling off at −0.37±0.15 and +0.29±0.17 µl for underpressure and overpressure, respectively, an average result of five gerbils. Our volume displacement values are somewhat on the large side, what could be explained by the same argument as given higher for the PT displacements. The PF bulged further inward at maximal positive EC pressure, causing the PF to come in contact with the malleus head.

Displacement of the pars flaccida at its center. The larger deformation found in the present experiments can also be seen when displacements of a single point at the center of the PF are compared. Averaging over G1 and G2, we found values of −520 µm at negative pressure and +450 µm at positive pressure.

Dirckx et al. (1997) found considerably smaller center displacements of −340 and +300 µm, respectively, for extreme pressure loads. Dirckx found a mean PF diameter of 1.54 mm, while we found a mean diameter of 1.40 mm. This slightly smaller diameter should give a smaller center displacement, not a larger one.

DISCUSSION

Tympanic membrane deformation measurements with X-ray CT versus moiré interferometry

For moiré, the TM had to be surgically exposed, while for CT, the TB was left intact. CT required about 30 min per scan, moiré measurements only seconds. The major difference was the ability of the CT technique to look inside the specimen, while moiré

FIG. 11. Four radial cross-sections (a–a′ to d–d′) of the PF were taken for extreme pressures of ±200 daPa and for the rest position. Points a, b, c, d, and a′ are at an edge with the bone, points b′, c′, and d′ are on the crease between PT and PF. For the negative EC pressure, the PF has a nearly symmetrical profile; for the positive pressure, the PF made contact with the malleus head, indenting the profile. At the crease, the boundary is not perfectly fixed.

could only measure the shapes of exposed surfaces. The two methods had comparable spatial resolution. For gerbil PT (Fig. 10) and PF (Fig. 11), the CT displacements were on the large side compared to our previous moiré measurements. The edge between PT and PF in the present measurements was found to be less rigid. Both observations may be caused by viscoelastic creep as explained above.

Let us remark also that, for the moiré measurements, the preparation had the tensor tympani muscle cut, the incudostapedial joint disarticulated, and the incus, stapes, and cochlea removed. The fact that this did not result in a large PT volume displacement agrees with the observation of Dirckx and Decraemer (2001) that, in gerbil, the displacement of the manubrium and TM remained unchanged from the intact ear even at this extensive stage of dissection (stage 3 in the cited paper).

For human, the present umbo displacements for TB2 were in good accord with values in the literature; TB1 had significantly larger displacements (Fig. 3). Creep cannot account for such a large difference; an exceptionally flaccid membrane might be responsible for these results.

Human

Pars tensa. In Dirckx and Decraemer (1991), cross-sections of the external surface of a pressurized human TM in directions along the manubrium and parallel to the manubrium were shown. The cross-sections of the PT for different pressures all converged to one point that was considered the functional edge. We could then not relate it to the position of the sulcus underneath. The extra information in the CT data (Figs. 4 and 5) shows clearly what happens at the annulus edge: the thick part of the AF inserted in the tympanic sulcus remains immobile and the deformations start at the thinner part where the AF gradually becomes TM.

Pars flaccida. In this study, the CT scan did not give good enough data to permit analysis of the human PF. Some of our older moiré results on TM displacement with static pressure can be used to complement this study. In a cross-section in a direction along the manubrium (Dirckx and Decraemer 1991), we see that, when the PF is pushed inward, it reclines superiorly more and more against the bony wall. When the PF is sucked outward, it gradually comes loose from the wall so that the apparent contact point moves up more superiorly. The functional edge point changes with pressure and the membrane hinges "instantaneously" about this sliding contact point. This mechanism is not in agreement with any fixed edge BC.

Gerbil

Pars tensa. Using projection phase-shift moiré, Dirckx and Decraemer (2001) measured the shape of the medial surface of gerbil TM after widely opening the bulla. Pressures of 0 and ±200 daPa were applied in the EC. The small peripheral ring with zero displacement present in the present gerbil data was overlooked in the moiré data as only a functional boundary was determined. This edge should coincide with the peripheral ring in the present experiments (Fig. 8) and exhibited a close to *simply supported* BC.

In the moiré paper, we showed that there was a sudden change in displacement of the TM at the edge with the manubrium, indicating a *simply supported* BC, which is also in accord with the present finding.

Pars flaccida. Real-time moiré was used in studies on the mechanical parameters of the PF (Dirckx et al. 1997, 1998). Locating the positions of fringes of consecutive order along a line in the images and connecting these points, we obtained rather coarsely defined cross-sections of the PF surface. Measurements were taken at the external surface and the functional edge was estimated but not the relation to the hidden bone underneath. PF deformation was modeled as a sphere cap which implicitly assumed that the PF was *simply supported* as we also concluded here.

Large static versus small acoustical displacements

Our study on TM BCs used static-pressure loads over a range that our ears are daily subjected to. Acoustic pressures are much smaller and vary rapidly in time. Can we draw conclusions about the BCs for acoustical pressures?

The material stiffnesses of soft tissues generally increase with the amplitude of the applied load (e.g., Decraemer et al. 1980; Wang et al. 2007) but, since this presumably applies to both the TM and the fibrocartilaginous ring, the relative stiffnesses probably do not change as much and the effect of amplitude on the boundary conditions may be small.

As for the effects of frequency, we found for human TM—in line with the findings of Fung (1972, 1981) for other soft biological tissues—that the stiffness (real part of the Young's modulus) increased by 50% over the wide frequency range of 0.01 to 100 Hz (Decraemer et al. 1980). The dissipative part (imaginary part of the Young's modulus) remained relatively small and almost constant over this frequency range. Assuming that we may extrapolate our results, the stiffness over the entire hearing range for most species would not even double.

Hence, *viscoelastic* effects are not expected to change the stiffness of the TM at the boundaries

drastically and hence possibly alter the choice of most appropriate BC. We have some experimental data to support this speculation. In an earlier experiment (Decraemer et al. 1997; Fay et al. 2005), we have measured vibration of the cat TM at closely spaced points (40 μ) along a line crossing the manubrium in the anterior to posterior direction. A pure-tone stimulus over a wide frequency range (0.1 to 23 kHz) was used. Observation was through the external EC and the observation direction was kept constant. Unfortunately, due to the overhang of the EC wall, the zone close to the annulus was not accessible and we have no record of the vibration at the peripheral TM boundary, but we do have measurements at the manubrial boundary. In Figure 12A, the displacement as a function of position along the line of observation points crossing the manubrium was plotted for different phases during the cycle. In Figure 12B, the displacements relative to the manubrium are plotted: from the displacements at points in the pars anterior, we subtracted the displacement of the anterior manubrium edge and, from the displacements at points in the posterior, we subtracted the displacement of the posterior edge. Displacements
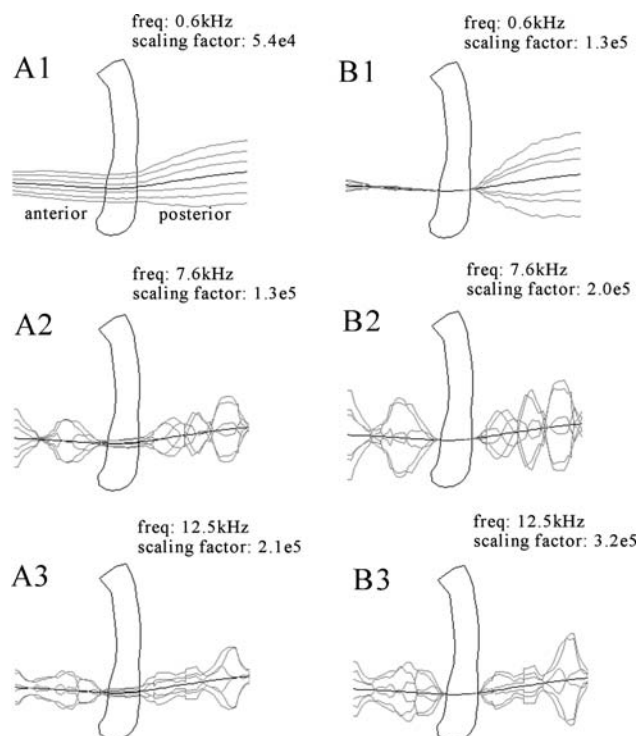
FIG. 12. In **A**, the displacement as a function of position along a line crossing the lower manubrium was plotted for six phases during the cycle (Decraemer et al. 1997; Fay et al. 2005). In **B**, the displacements relative to the manubrium are plotted in a similar way: for the points in the pars anterior, the displacement of the anterior manubrium edge was subtracted; for the points in the posterior, the displacement of the posterior edge. Displacements were scaled up by the annotated scaling factor to visualize them in the millimeter scale of the plot of the manubrium.

were magnified by a scaling factor to make them visible on the millimeter scale of the 3D plot of the manubrium; these factors, which are different for different frequencies, are annotated on the plots. We show data at three frequencies. At low frequencies (e.g., 585 Hz; Fig. 12A1), the TM is in its fundamental mode and the vibration phases of the manubrium and points on the TM are the same. At higher frequencies (7.6 kHz, Fig. 12A2 and 12.5 kHz, Fig. 12A3), the mode of vibration has changed and the vibration pattern has broken up. In all the B panels of Figure 12, we see how the relative displacement of the TM at the edges of the manubrium supports a *simply supported* condition within the limits of the measurement uncertainty. This is exactly what we have concluded in both human and gerbil based on our static-pressure experiment. That this is true up to the highest frequency indicates that inertial effects do not seem to change the edge behavior.

Boundary conditions in mathematical models

We have studied the deformation at the boundaries of the TM in detail to learn how the attachment of the TM to its boundaries behaves under static pressure and how this behavior can be described in mathematical terms. In principle, a mathematical model could be refined to such a high degree—e.g., specifying all components and their interconnections to a level where fibers connecting the AF to the tympanic sulcus are included—that the model replicates and describes the real situation perfectly. In practice, however, the model is simplified at the edge and some kind of boundary condition is assigned.

Many mathematical middle-ear models have used simply supported, fully clamped, or a combination for the boundary conditions of the TM (Funnell 1975; Funnell and Laszlo 1978; Funnell et al. 1987, 1992; Funnell and Decraemer 1996; Rabbitt & Holmes 1986; Ladak & Funnell 1996; Beer et al. 1996, 1999; Fay et al. 2006; Elkhouri et al. 2006; Eiber et al. (2000); Ladak et al. 2006; Qi et al. 2008). Changing a model from simply supported to fully clamped boundary conditions may cause differences in response that, depending on the characteristics of the model and the magnitude of the applied load, may be more or less important. For a flat circular structure like the pars flaccida in gerbil, the formulae for a flat circular plate given by Roark and Young (1975; cases 10a and 10b in Table 24 with r0=0) predict increases of the displacement at the center by factors of around 4 when small (acoustic) pressures are applied.

Other middle-ear models have included more explicit representations of the connection between the TM and the bony annulus. Van Wijhe (2001) modeled the AF with reasonable Young's moduli and

concluded that it was effectively rigid, thus justifying the use of clamped boundary condition for the TM. Homma et al. (2009) also explicitly modeled the AF but did not discuss its effect. Wada et al. (1992) added springs at the TM boundary without direct evidence that the corresponding part of the TM really moves, and several other models have also used springs (Williams et al. 1996; Prendergast et al. 1999; Koike et al. 2002). Gan et al. (2002) and Sun et al. (2002) represented the coupling between the eardrum and the tympanic annulus boundary by using elements that were approximately five times softer than the remainder of the elements representing the pars tensa. We see that different ideas about how to describe the boundaries mathematically have been adopted. One main problem was that no specific experimental data were available describing the TM behavior at its edges. The present data are an attempt to address this lack.

CONCLUSIONS

In finite element models of the TM, it is common to use thin-shell elements and to apply either *simply supported* or *fully clamped* mathematical boundary conditions. We found that judged by the deformation at the edges with static pressures, the choice is not so straightforward and it is hard to decide a priori which of these conditions will optimally describe the experimental results.

For gerbil, the choice of a *simply supported* boundary condition for the pars flaccida at the edge with the bony ledge and for the pars tensa at the edge with the manubrium is straightforward on the basis of the displacement at the edge as measured with CT. At the crease between pars flaccida and pars tensa and at the pars tensa edge, the situation is not so clear. The thickness of the TM shows a small bulge close to the AF and deformation only started at the inner side of this bulge.

In human, the deformation of the AF is that of a thick wedge of material that bends considerably at its tip where the AF blends into the TM, but that is not deformed at its thick end where it is held fixed in the tympanic sulcus. Choosing a boundary condition here is not easy, and a more detailed modeling of the structures here is probably required. This holds also at the edge between TM and manubrium where we also have a complicated boundary due to the interposition of the plica mallearis. In human, the pars flaccida makes more and more contact with the underlying bone as the EC pressure increases and is pulled loose from this bone for negative pressures, a situation which is not readily described by any simple boundary condition. To give firmer answers about how to model the deformation at the boundaries, the thicker ring in gerbil and the exact shapes of the AF and tympanic sulcus should be included in the finite element model in order to come to a decision about which model best replicates the present experimental data. We defer this to a follow-up finite element study where we will model more generally all of our present results.

ACKNOWLEDGEMENTS

REFERENCES

ANSON BJ, DONALDSON JA (1981) Surgical anatomy of the temporal bone. Saunders, Philadelphia

BEER HJ, BORNITZ M, DRESHER J, SCHMIDT R, HARDTKE HJ (1996) Finite element modeling of the human eardrum and applications. In: Hüttenbrink KB (ed) Proceedings of the Middle Ear Mechanics in Research and Otosurgery, Dresden, pp 40–47

BEER HJ, BORNITZ M, HARDTKE HJ, SCHMIDT R, HOFMANN G, VOGEL U, ZAHNERT T, HÜTTENBRINK KB (1999) Modeling of components of the human middle ear and simulation of their dynamic behaviour. Audiol Neurootol 4:155–162

DECRAEMER WF, KHANNA SM (2004) Measurement, visualization and quantitative analysis of complete three-dimensional kinematical data sets of human and cat middle ear. In: Gyo K, Wada H, Hato N, Koike T (ed) Proceedings of the 3rd Symposium on Middle Ear Mechanics in Research and Otology, World Scientific, pp 3–10

DECRAEMER WF, MAES MA, VANHUYSE VJ, VANPEPERSTRAETE P (1980) A non-linear viscoelastic constitutive equation for soft biological tissues, based upon a structural model. J Biomech 13:559–564

DECRAEMER WF, KHANNA SM, FUNNELL WRJ (1997) Vibrations of the cat tympanic membrane measured with high spatial resolution. Abstract. Proceedings of the 20th Midwinter Research Meeting of the Association for Research in Otolaryngology, p 48

DECRAEMER WF, KHANNA SM, DIRCKX JJJ (2002) The integration of detailed 3-dimensional anatomical data for the quantitative description of 3-dimensional vibration of a biological structure. An illustration from the middle ear. In: Tomasini EP (ed) Vibration measurements by laser techniques: advances and applications. SPIE 4827, pp 148–158

DECRAEMER WF, FUNNELL WRJ, DIRCKX JJJ (2003) Three-dimensional modeling of the middle-ear ossicular chain using a commercial high-resolution X-ray CT scanner. JARO 2:250–263

DIRCKX JJJ, DECRAEMER WF (1991) Human tympanic membrane deformation under static pressure. Hear Res 51:93–106

DIRCKX JJJ, DECRAEMER WF (2001) Effect of middle ear components on eardrum quasi-static deformation. Hear Res 157:124–137

DIRCKX JJJ, DECRAEMER WF (2003) Moiré topography for basic and clinical hearing research. Recent Res Devel Optics 3:271–296

DIRCKX JJJ, DECRAEMER WF (2004) Real-time moiré topography, chapter 12.1. In: Walker CA (ed) Handbook of moiré measurements. Series in optics and optoelectronics. Institute of Physics, Philadelphia, pp 287–396

DIRCKX JJJ, DECRAEMER WF, VON UNGE M, LARSSON CH (1997) Measurement and modeling of the boundary shape and surface deformation of the Mongolian pars flaccida. Hear Res 111:153–164

DIRCKX JJJ, DECRAEMER WF, VON UNGE M, LARSSON CH (1998) Volume displacement of the gerbil eardrum pars flaccida as a function of middle ear pressure. Hear Res 118:35–45

EIBER A, FREITAG HG, SCHIMANSKI G, ZENNER HP (2000) On the coupling of prostheses to the middle ear structure and its influence on sound transfer. In: Rosowski J, Merchant S (eds) The function and mechanics of normal and diseased middle ears. Kugler, The Hague, pp 297–308

ELKHOURI N, LIU H, FUNNELL WRJ (2006) Low-frequency finite-element modelling of the gerbil middle ear. JARO 7:399–411

FAY JP, PURIA S, DECRAEMER WF, STEELE CR (2005) Three approaches for estimating the elastic modulus of the tympanic membrane. J Biomech 38:1807–1815

FAY JP, PURIA S, STEELE CR (2006) The discordant eardrum. PNAS 103(52):19743–19748

FUNG Y (1972) Biomechanics, its foundations and objectives. Prentice-Hall, Englewood Cliffs

FUNG Y (1981) Biomechanics: mechanical properties of living tissues. Springer, New York

FUNNELL WRJ (1975) A theoretical study of eardrum vibrations using the finite-element method. Ph.D. thesis, McGill University, Montreal

FUNNELL WRJ, DECRAEMER WF (1996) On the incorporation of moiré shape measurements in finite-element models of the cat eardrum. J Acoust Soc Am 100(1):925–932

FUNNELL WRJ, LASZLO CA (1978) Modeling of the cat eardrum as a thin shell using the finite-element method. J Acoust Soc Am 63(5):1461–1467

FUNNELL WRJ, DECRAEMER WF, KHANNA SM (1987) On the damped frequency response of a finite-element model of the cat eardrum. J Acoust Soc Am 81(6):1851–1859

FUNNELL WRJ, KHANNA SM, DECRAEMER WF (1992) On the degree of rigidity of the manubrium in a finite-element model of the cat eardrum. J Acoust Soc Am 91(4):2082–2090

GAN RZ, SUN Q, DYER RK, CHANG KH, DORNER KJ (2002) Three dimensional modelling of middle ear biomechanics and its applications. Otol Neurotol 23:271–280

GEA SLR, DECRAEMER WF, DIRCKX JJJ (2005) Region of interest micro-CT of the middle-ear: a practical approach. J X-ray Sci Tech 6(3):223–233

GRAHAM MD, REAMS C, PERKINS R (1978) Human tympanic membrane-malleus attachment. Ann Otol Rhinol Laryngol 87:426–431

GULYA AJ, SCHUKNECHT HF (1995) Anatomy of the temporal bone with surgical implications. The Parthenon, New York

HENSON MM, MADDEN VJ, RASK-ANDERSEN H, HENSON OW JR (2005) Smooth muscle in the annulus fibrosis of the tympanic membrane in bats, rodents, insectivores, and humans. Hear Res 200:29–37

HOMMA K, DU Y, SHIMIZU Y, PURIA S (2009) Ossicular resonance modes of the human middle ear for bone and air conduction. J Acoust Soc Am 125:968–979

HÜTTENBRINK KB (1988) The mechanics of the middle-ear at static pressures. Acta Otolaryngol Suppl 451:1–35

KOIKE T, WADA H, KOBAYASHI T (2002) Modeling of the human middle ear using the finite-element method. J Acoust Soc Am 111:1306–1317

KUIJPERS W, PETERS TA, TONNAER ELGM (1999) Nature of the tympanic membrane insertion into the tympanic bone of the rat. Hear Res 128:80–88

KUYPERS LC, DIRCKX JJJ, DECRAEMER WF, TIMMERMANS JP (2005) Thickness distribution of fresh eardrums of cat obtained with confocal microscopy. JARO 6(3):223–233

KUYPERS LC, DECRAEMER WF, DIRCKX JJJ (2006) Thickness distribution of fresh and preserved human eardrums measured with confocal microscopy. Otol Neurotol 27(2):256–264

LADAK HM, FUNNELL WRJ (1996) Finite-element modeling of the normal and surgically repaired cat middle ear. J Acoust Soc Am 100(2):933–944

LADAK HM, FUNNELL WRJ, DECRAEMER WF, DIRCKX JJJ (2006) A geometrically nonlinear finite-element model of the cat eardrum. J Acoust Soc Am 119(5):2859–2868

LIM DJ (1968a) Tympanic membrane. Electron microscopic observation. Part I: pars tensa. Acta Otolaryngol 66:181–198

LIM DJ (1968b) Tympanic membrane. Part II: pars flaccida. Acta Otolaryngol 66:515–532

LIM DJ (1970) Human tympanic membrane. Acta Otolaryngol 70:176–186

LIM DJ (1995) Structure and function of the tympanic membrane: a review. Acta Otorhinolaryngol Belg 49:101–115

POLITZER A (1892) The anatomical and histological dissection of the human ear in the normal and diseased condition. Baillière, Tindall and Cox, London Translated from the German by George Stone

PRENDERGAST PJ, FERRIS P, RICE HJ, BLAYNEY AW (1999) Vibro-acoustic modeling of the outer and middle ear using the finite element method. Audiol Neurootol 4:185–191

QI L, FUNNELL WRJ, DANIEL DS (2008) A nonlinear finite-element model of the newborn middle ear. J Acoust Soc Am 124:337–347

RABBITT RD, HOLMES MH (1986) A fibrous dynamic continuum model of the tympanic membrane. J Acoust Soc Am 80:1716–1728

ROARK RJ, YOUNG WC (1975) Formulas for stress and strain, 5th edn. McGraw-Hill, New York xvi + 624 pp

RUAH CB, SCHACHERN PA, ZELTERMAN D, PAPARELLA MM, YOON TH (1991) Age-related morphologic changes in the human tympanic membrane. Arch Otolaryngol Head Neck Surg 117:627–634

SHIMADA T, LIM DJ (1971) The fiber arrangement of the human tympanic membrane: a scanning electron microscopic observation. Ann Otol Rhinol Laryngol 80:210–217

SUN Q, GAN RZ, CHANG KH, DORNER KJ (2002) Computer-integrated finite element modeling of human middle ear. Biomech Model Mechanobiol 1:109–122

UNO Y (2000) The attachment structure of the guinea pig tympanic membrane. Auris Nasus Larynx 27:45–50

VAN WIJHE RG (2001) A finite-element model of the middle ear of the moustached bat. M.Eng. thesis, McGill University. Available at http://escholarship.mcgill.ca

VON UNGE M, BAGGER-SJÖBACK D, BORG E (1991) Mechanoacoustic properties of the tympanic membrane: a study on isolated Mongolia gerbil temporal bones. Am J Otol 12(6):407–419

VON UNGE M, DECRAEMER WF, DIRCKX JJ, BAGGER-SJÖBACK D (1993) Displacement of the gerbil tympanic membrane under static pressure variations measured with real-time differential moiré interferometry. Hear Res 70:229–242

WADA H, METOKI T, KOBAYASHI T (1992) Analysis of dynamic behavior of human middle ear using a finite-element method. J Acoust Soc Am 92:3157–3168

WANG X, CHENG T, GAN RZ (2007) Finite-element analysis of middle-ear pressure effects on static and dynamic behavior of human ear. J Acoust Soc Am 122:906–917

WILLIAMS KR, BLANEY AW, RICE HJ (1996) Development of a finite element model of the middle ear. Rev Laryngol Otol Rhinol (Bord) 117:259–264

YANG X, HENSON OW (2002) Smooth muscle in the annulus fibrosis of the tympanic membrane: physiological effects on sound transmission in the gerbil. Hear Res 164:104–114